

Spin-valley dynamics of electrically driven ambipolar carbon-nanotube quantum dots

E.N. Osika,¹ A. Chacón,² M. Lewenstein,^{2,3} and B. Szafran¹

¹*AGH University of Science and Technology, Faculty of Physics and Applied Computer Science,
al. Mickiewicza 30, 30-059 Kraków, Poland*

²*ICFO - Institut de Ciències Fotoniques, The Barcelona Institute
of Science and Technology, 08860 Castelldefels (Barcelona), Spain*

³*ICREA, Pg. Lluís Companys 23, 08010 Barcelona, Spain*

An ambipolar n - p double quantum dot defined by potential variation along a semiconducting carbon-nanotube is considered. We focus on the $(1e,1h)$ charge configuration with a single excess electron in the conduction band state confined in the n -type dot and a single missing electron in the valence band state of the p -dot for which lifting of the Pauli blockade of the current was observed in the electric-dipole spin resonance [E. A. Laird et al. Nat. Nanotech. 8, 565 (2013)]. The dynamics of the system driven by periodic electric field is studied with the Floquet theory and the time-dependent configuration interaction method with the single-electron spin-valley-orbitals determined for atomistic tight-binding Hamiltonian. We find that the transitions lifting the Pauli blockade are strongly influenced by coupling to a vacuum state with an empty n dot and a fully filled p dot. The coupling shifts the transition energies and strongly modifies the effective g factors for axial magnetic field. The coupling is modulated by the bias between the dots but it appears effective for surprisingly large energy splitting between the $(1e,1h)$ ground state and the vacuum $(0e,0h)$ state. Multiphoton transitions and high harmonic generation effects are also discussed.

I. INTRODUCTION

Manipulation of the spin degree of freedom for electrons confined in quantum dots (QDs) has been under extensive studies in the context of construction of spintronic single-electron devices [1] for over a decade. For QDs a successful implementation of the electron spin-resonance was performed with a microwave generator integrated into the device [2]. The magnetic field produced by ac currents [2] was soon replaced by the effective magnetic field due to the spin-orbit coupling for a driven electron motion within the QD [3–5], in the electric-dipole spin resonance [6] (EDSR). EDSR can also be induced by fluctuations of the Overhauser field [7] or inhomogeneous field [8] translated into an effective ac magnetic field averaged by the wave function of a periodically driven electron [9]. The detection of the spin flip [2–5, 7] exploits the Pauli blockade [10] of the current that flows across a double QD.

The lifting of the Pauli blockade induced by ac electric field has been observed in double QDs defined within a semiconducting carbon nanotube (CNT) [11, 12], where the electron dynamics involves both the spin and the valley [13] degree of freedom. The EDSR was observed for double QDs in an ambipolar work point: with one quantum dot storing an extra electron of the conduction band and the other a hole (a single-unoccupied state) in the valence band – denoted as $(1e,1h)$ in the following. The energy spectrum of the $(1e,1h)$ system was determined with the atomistic tight binding approach in Ref. [14]. The driven electron dynamics was discussed in Ref. [15] in a continuum approach strictly in the subspace corresponding to the $(1e,1h)$ charge configuration. The dynamics of the $(1e,1e)$ system in double carbon nanotube unipolar dots has also been considered [16].

The quantum dot confined single-electron states are

nearly fourfold degenerate with a pair of spin-valley doublets split by spin-orbit coupling energy of the order of 1 meV [17], so that the dynamics of the system in the experimental work point [11, 12] involves a single electron in the n dot and three electrons in the p dot. In this work we solve the problem of the spin-valley transitions between the Pauli blocked and nonblocked states using a time dependent configuration interaction approach and Floquet theory [18, 19] for the ambipolar dots. We find that the states of the $(1e,1h)$ charge configuration are strongly coupled by the ac potential with the “vacuum state” $(0e,0h)$ – with an empty n -dot and fully filled p -dot, even when its energy is relatively high above the $(1e,1h)$ ground state. The coupling – beyond the subspace considered in Ref. [15] – produces a strong shift of the transition lines off the energy spectra, which for axial magnetic field strongly modifies the effective g factors for the driven spin-valley transitions.

The present approach – that provides exact result for the coherent few-electron dynamics including the higher order effects – besides energy shifts describes also the multiphoton transitions [4, 11, 20, 21]. The dynamics of QDs in external ac voltages enters the regime of strongly driven systems already at relatively weak voltages. Motivated by this fact we look for the high harmonic generation (HHG) effects that are encountered in systems

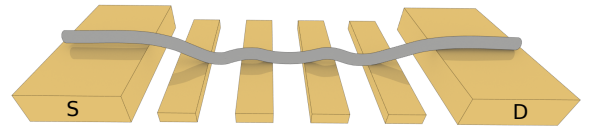


Figure 1. Schematics of the considered system – carbon nanotube deflected above electrostatic gates forming the QD confinement potential.

driven by strong laser fields (for HHG from atomic or molecular sources see [22, 23], for recent studies of HHG in solids see [24–27]). Higher harmonics of the driven dipole moment are found but only in resonant conditions.

II. THEORY

A. Model

In this section we first discuss a model, describing a n - p quantum dot induced within a carbon nanotube. In the next section (B) we present the method that we use to describe the dynamics of the system: time-dependent configuration interaction approach. Finally, in section C we discuss the Floquet approach, specifically suited for the treatment of the time-dependent problems with periodic time modulations.

We consider a carbon nanotube of length $L = 53.11$ nm, diameter $2r = 1.33$ nm, with the chiral vector $C_h = (17, 0)$ for which the CNT is semiconducting and can confine electrons in quantum dots defined electrostatically. The nanotube is considered bent [28] above the electrostatic gates as in Fig. 1 and in the experiment [see Fig. 2(a) of Ref. 12]. We have found [14] that the bends of the CNT appearing at the area where the confinement potential is defined on the gates results in energy spectra which qualitatively agree with the experimental spectrum of transitions lifting the Pauli spin-valley blockade of the current [12].

The global z axis of the chosen coordinate system coincides with the axis of the straight part of the CNT axis [Fig. 2]. The nanotube is deflected within the global xz -plane. The radii of the bends in Fig. 2 are $R_n = 8$ nm and $R_p = 11$ nm. The positions of the centre of the arcs along the z direction are $d_n = 8$ nm and $d_p = 11$ nm, respectively. Locally the bend is parametrized by the inclination angle ϕ_i of CNT axis (for i -th ion) to the global z axis [see the inset to Fig. 2].

We model a double n - p quantum dot induced within the nanotube by external voltages. The shape of the electrostatic confinement potential is described by

$$W_{QD}(z) = -\frac{V_n}{1 + \left(\frac{z+z_s}{d}\right)^{14}} + \frac{V_p}{1 + \left(\frac{z-z_s}{d}\right)^{14}}, \quad (1)$$

where V_n and V_p are potentials on the n and p dots, respectively, z_s is a shift of the QD centre from $z = 0$ and d is a half width of the QD. In the calculations we use $V_n = V_p = 0.21$ eV, $z_s = 8$ nm and $2d = 16$ nm. The experimental data [12] contain signatures of the intervalley mixing. We account for the intervalley scattering introducing a potential peak of 1 eV at a single atom at $z = -12.28$ nm which is responsible for the mixing of the K and K' orbital states. In part of the calculations [Section IV.D] an additional bias electric field F_b is introduced. The resulting electrostatic potential is described by $W_b(z) = eF_b z$ for $z \in [-2d, 2d]$,

$W_b(z) = W_b(-2d)$ for $z < -2d$ and $W_b(z) = W_b(2d)$ for $z > 2d$.

We apply the external magnetic field within the xz plane, of the magnitude B and the orientation defined by an angle α that it forms with the z axis: $\mathbf{B} = (B_x, 0, B_z) = (B \sin \alpha, 0, B \cos \alpha)$.

B. Time-dependent configuration interaction approach

In order to study the spin-valley dynamics of the confined carriers we *i*) calculate the single electron energy spectrum, *ii*) solve the Schrödinger equation for the few-electron states with the Slater determinant basis built from the single-electron eigenstates, *iii*) solve the time-dependent Schrödinger equation in the basis of the few electron eigenstates under the influence of the ac electric field. The results presented below provide an exact solution of the dynamics of the system composed of four electrons in states near the Fermi level.

In order to determine the single-electron states we use the atomistic tight-binding approach with the p_z orbitals. We solve the eigenproblem of Hamiltonian

$$H_{1e} = \sum_{\{i,j,\sigma,\sigma'\}} (c_{i\sigma}^\dagger t_{ij}^{\sigma\sigma'} c_{j\sigma'} + h.c.) + \sum_{i,\sigma,\sigma'} c_{i\sigma}^\dagger \left((W_{QD}(\mathbf{r}_i) + W_b(\mathbf{r}_i)) \delta_{\sigma\sigma'} + \frac{g_L \mu_b}{2} \boldsymbol{\sigma}^{\sigma\sigma'} \cdot \mathbf{B} \right) c_{i\sigma'}. \quad (2)$$

The first sum in Eq. (2) accounts for the hopping between the nearest neighbor atoms. It runs over the p_z spin-orbitals of the nearest neighbor pairs of atoms, $c_{i\sigma}^\dagger (c_{i\sigma})$ is the particle creation (annihilation) operator at ion i with spin σ , and $t_{ij}^{\sigma\sigma'}$ is the spin-dependent hopping parameter. The second sum accounts for the external electric and magnetic fields, with $\delta_{\sigma\sigma'}$ standing for the Kronecker delta, $g_L = 2$ for the Landé factor, μ_b the Bohr magneton and $\boldsymbol{\sigma}$ for the vector of Pauli matrices.

In carbon nanotubes QDs [17, 29–31] the control over the spin is provided by mixing of the π and σ bonds that allows the carbon atomic spin-orbit coupling effects to appear in the electron band-structure [17, 32–36]. The spin-orbit interaction due to the curvature of the graphene plane introduces the spin dependence and spin mixing in the hopping parameters $t_{ij}^{\sigma\sigma'}$. We apply the form of the parameters that accounts for both the folding of the graphene plane into the tube [35] and the curvature of the tube as a whole [37],

$$\begin{aligned} t_{ij}^{\uparrow\uparrow} &= (z_i | H | z_j) + i\delta \cos \phi_j (z_i | H | x_j) - i\delta \cos \phi_i (x_i | H | z_j) + i\delta \sin \phi_j \sin \theta_j (z_i | H | y_j) - i\delta \sin \phi_i \sin \theta_i (y_i | H | z_j), \\ t_{ij}^{\downarrow\downarrow} &= (z_i | H | z_j) - i\delta \cos \phi_j (z_i | H | x_j) + i\delta \cos \phi_i (x_i | H | z_j) - i\delta \sin \phi_j \sin \theta_j (z_i | H | y_j) + i\delta \sin \phi_i \sin \theta_i (y_i | H | z_j), \\ t_{ij}^{\uparrow\downarrow} &= -i\delta \sin \phi_j (z_i | H | x_j) + i\delta \sin \phi_i (x_i | H | z_j) - \delta (\sin^2 \frac{\phi_j}{2} e^{i\theta_j} + \cos^2 \frac{\phi_j}{2} e^{-i\theta_j}) (z_i | H | y_j) + \delta (\sin^2 \frac{\phi_i}{2} e^{i\theta_i} + \cos^2 \frac{\phi_i}{2} e^{-i\theta_i}) (x_i | H | y_j) \end{aligned}$$

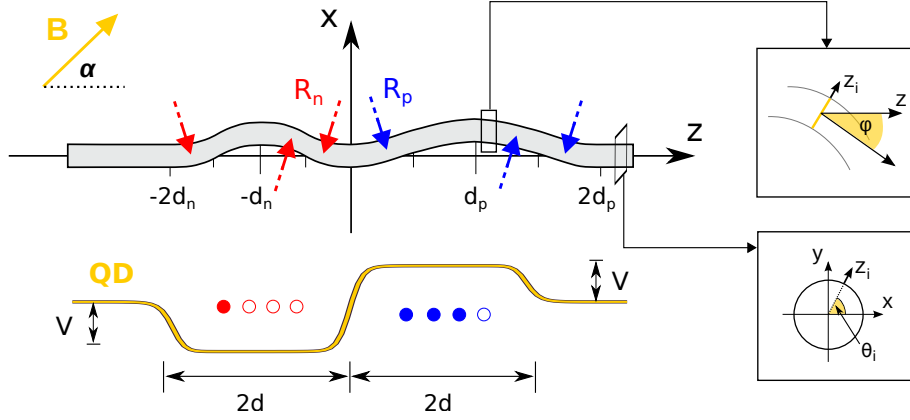


Figure 2. Schematics of the modeled CNT with all the dimensions and coordinate systems used in the calculations explained.

$$\cos^2 \frac{\phi_i}{2} e^{-i\theta_i} (y_i | H | z_j),$$

and

$$t_{ij}^{\uparrow\downarrow} = -i\delta \sin \phi_j (z_i | H | x_j) + i\delta \sin \phi_i (x_i | H | z_j) + \delta (\sin^2 \frac{\phi_j}{2} e^{-i\theta_j} + \cos^2 \frac{\phi_j}{2} e^{i\theta_j}) (z_i | H | y_j) - \delta (\sin^2 \frac{\phi_i}{2} e^{-i\theta_i} + \cos^2 \frac{\phi_i}{2} e^{i\theta_i}) (y_i | H | z_j),$$

where $(\gamma_i | H | \gamma_j) = V_{pp}^\pi \mathbf{n}(\gamma_i) \cdot \mathbf{n}(\gamma_j) + (V_{pp}^\sigma - V_{pp}^\pi) \frac{(\mathbf{n}(\gamma_i) \cdot \mathbf{R}_{ji})(\mathbf{n}(\gamma_j) \cdot \mathbf{R}_{ji})}{|\mathbf{R}_{ji}|^2}$, $\gamma = x, y$ or z , γ_i stands for the orbital of ion at \mathbf{R}_i position and $\mathbf{n}(\gamma_i)$ is a unit vector in the direction of orbital γ_i . In the calculations we use the tight-binding Slater-Koster parameters $V_{pp}^\pi = -2.66$ eV, $V_{pp}^\sigma = 6.38$ eV [38] and the spin-orbit coupling parameter $\delta = 0.003$ [34, 35]. The interaction of the magnetic field with the orbital magnetic moments is taken into account by the Peierls phase

$$t_{ij}^{\sigma\sigma'}(B) = t_{ij}^{\sigma\sigma'}(0) \exp(i \frac{2\pi}{\Phi_0} \int_{\mathbf{r}_i}^{\mathbf{r}_j} \mathbf{A} \cdot d\mathbf{l}),$$

where $\Phi_0 = h/e$ is the flux quantum, $\mathbf{B} = \nabla \times \mathbf{A}$, and the Landau gauge $\mathbf{A} = (0, B_z x, B_x y)$ is applied.

With the single-electron problem solved, we calculate the few electron eigenstates using the configuration interaction (CI) method. We are interested in (1e, 1h) charge configuration, in which in the n -type dot we have a single-electron (1e) in the conduction band and three electrons (or a single unoccupied state 1h) in the p -type dot (see Fig. 2). Figure 3(a) shows the single-electron energy spectrum as a function of the potential $V = V_n = V_p$. All the energy levels plotted in Fig. 3 are nearly fourfold degenerate with respect to the valley and spin. For the calculations we adopt $V = 0.21$ eV and take into the basis several lowest-energy levels of the conduction band [the red curves in Fig. 3(b)] as well as the highest energy level of the valence band [the uppermost blue curve in Fig. 3(a)]. We assume that all the energy levels below are fully occupied and do not participate in the dynamics of the system, which is governed by the behavior of the last four electrons.

The Hamiltonian for the interacting electron system

reads

$$H_{4e} = \sum_a \epsilon_a g_a^\dagger g_a + \frac{1}{2} \sum_{abcd} V_{ab;cd} g_a^\dagger g_b^\dagger g_c g_d, \quad (3)$$

where ϵ_a is the energy of the a -th eigenstate of Hamiltonian H_{1e} while g_a^\dagger and g_a are the creation and annihilation operators of the electron in the a -th state. The electron-electron interaction is taken into account in the second term of Eq. (3) with the matrix elements

$$\begin{aligned} V_{ab;cd} &= \langle \psi_a(\mathbf{r}_1, \sigma_1) \psi_b(\mathbf{r}_2, \sigma_2) | H_c | \psi_c(\mathbf{r}_1, \sigma_1) \psi_d(\mathbf{r}_2, \sigma_2) \rangle \\ &= \sum_{i, \sigma_i; j, \sigma_j; k, \sigma_k; l, \sigma_l} \beta_{i, \sigma_i}^{a*} \beta_{j, \sigma_j}^{b*} \beta_{k, \sigma_k}^c \beta_{l, \sigma_l}^d \delta_{\sigma_i; \sigma_k} \delta_{\sigma_j; \sigma_l} \times \\ &\quad \langle p_z^i(\mathbf{r}_1) p_z^j(\mathbf{r}_2) | H_c | p_z^k(\mathbf{r}_1) p_z^l(\mathbf{r}_2) \rangle, \end{aligned} \quad (4)$$

where H_c is the electron-electron interaction potential

$$H_C = \frac{e^2}{4\pi\epsilon_0 r_{12}}$$

with $r_{12} = |\mathbf{r}_1 - \mathbf{r}_2|$ and the dielectric constant $\epsilon = 9$ as for Al_2O_3 – material which has been used as a substrate in the experimental setups [12]. The coefficients β_{i, σ_i}^a define contributions of p_z^i orbitals of spin σ_i to the single-electron eigenstate a . In the calculations we use the two-center approximation [39]. The on-site integral ($i = j$) we approximate by $\langle p_z^i p_z^j | \frac{e^2}{4\pi\epsilon_0 r_{ij}} | p_z^i p_z^j \rangle = 16.522$ eV [40] and for $i \neq j$ we use the formula $\langle p_z^i p_z^j | \frac{1}{r_{ij}} | p_z^k p_z^l \rangle = \frac{1}{r_{ij}} \delta_{ik} \delta_{jl}$ [41]. The atomistic approach used here accounts for all intervalley effects [42] that accompany the short range component of the Coulomb potential. Moreover, the present approach is not limited by the low-energy continuum approximation, and covers an ample variation of the external potential necessary for formation of an ambipolar quantum dot within the tube.

The energy spectrum is given in Fig. 3(b) as a function of the bias field. The slope of the lines is determined by the electric dipole moment of the system i.e., the electron distribution between the dots. The ground-state corresponds to the (1e, 1h) charge configuration that is

focused below. The nonzero bias field is considered in Section IV.D, elsewhere we take $F_b = 0$.

We simulate the valley and spin transitions driven by external ac field by solving the time-dependent Schrödinger equation with Hamiltonian

$$H'(t) = H_{4e} + \sum_{j=1}^4 eF_0 z_j \sin(\omega t), \quad (5)$$

where F_0 is the ac electric field amplitude and ω is its frequency. Using the eigenstates Ψ_n of Hamiltonian H_{4e} we construct basis in which the time-dependent Schrödinger equation is solved

$$\Psi(\mathbf{r}_{1\dots 4}, \boldsymbol{\sigma}_{1\dots 4}, t) = \sum_n c_n(t) \Psi_n(\mathbf{r}_{1\dots 4}, \boldsymbol{\sigma}_{1\dots 4}, t) e^{-\frac{iE_n t}{\hbar}}. \quad (6)$$

In this basis the Schrödinger equation $i\hbar \frac{\partial \Psi}{\partial t} = H' \Psi$ takes the form

$$i\hbar \dot{c}_k(t) = \sum_n c_n(t) eF_0 \sin(\omega t) \langle \Psi_k | z | \Psi_n \rangle e^{-\frac{i(E_n - E_k)t}{\hbar}}. \quad (7)$$

We discretize the time in equation (7) and calculate the coefficients $c_k(t)$ using the Crank-Nicolson algorithm.

C. Floquet approach

The direct solution of the time-dependent Schrödinger method is supported with the Floquet theory. We use the Floquet Hamiltonian method [18, 19] to describe the dynamics of the system. For Hamiltonian $H'(t)$ that is periodic in time with the period $T = 2\pi/\omega$, the Floquet theorem asserts the existence of the solution of the Schrödinger equation

$$i\hbar \frac{\partial \Psi}{\partial t} = H' \Psi \quad (8)$$

of the form

$$\Phi(t) = \phi(t) e^{-i\epsilon t/\hbar}, \quad (9)$$

where $\phi(t)$ is periodic in time. The Φ functions are called quasienergy eigenstates (QES) and upon the Fourier series expansion can be expressed by

$$\Phi_\alpha = e^{-i\epsilon_\alpha t/\hbar} \sum_{n=-\infty}^{\infty} \sum_{\beta} v_{\alpha\beta}^{(n)} e^{-in\omega t} |\beta\rangle, \quad (10)$$

where α enumerates the quasi-energy state, ϵ_α is the quasienergy, β are eigenfunctions of the Hamiltonian H_{4e} and $v_{\alpha\beta}^{(n)}$ are coefficients expanding the quasi-energy state in the basis of β eigenstates. Since functions Φ_α satisfy the equation $(H' - i\hbar \frac{\partial}{\partial t})\Phi_\alpha = 0$, after expanding it in the basis of β eigenstates we obtain

$$\sum_n \sum_{\beta} [\langle \alpha | H'^{(m-n)} | \beta \rangle - (\epsilon_\alpha + m\omega) \delta_{mn} \delta_{\alpha\beta}] v_{\alpha\beta}^{(n)} = 0, \quad (11)$$

where

$$H'^{(n)} = \frac{1}{T} \int_0^T H'(t) e^{in\omega t} dt. \quad (12)$$

For the case of the perturbation $eF_0 z \sin(\omega t)$ the matrix elements $\langle \alpha | H'^{(m-n)} | \beta \rangle$ read

$$\begin{aligned} \langle \alpha | H'^{(m-n)} | \beta \rangle &= E_\alpha \delta_{\alpha\beta} \delta_{mn} + \frac{i}{2} \delta_{m-n,1} \langle \alpha | eF_0 z | \beta \rangle + \\ &- \frac{i}{2} \delta_{m-n,-1} \langle \alpha | eF_0 z | \beta \rangle. \end{aligned} \quad (13)$$

Finally, one writes the time-independent Floquet Hamiltonian H_F with the matrix elements defined by

$$\langle \alpha m | H_F | \beta n \rangle = \langle \alpha | H'^{(m-n)} | \beta \rangle + n\hbar\omega \delta_{\alpha\beta} \delta_{mn} \quad (14)$$

in a block form we can express the matrix of the Hamiltonian H_F as

$$\begin{bmatrix} \ddots & \dots & \dots & \dots & \dots & \dots & \ddots \\ \vdots & A + 2\hbar\omega I & B & 0 & 0 & 0 & \vdots \\ \vdots & -B & A + \hbar\omega I & B & 0 & 0 & \vdots \\ \vdots & 0 & -B & A & B & 0 & \vdots \\ \vdots & 0 & 0 & -B & A - \hbar\omega I & B & \vdots \\ \vdots & 0 & 0 & 0 & -B & A - 2\hbar\omega I & \vdots \\ \ddots & \dots & \dots & \dots & \dots & \dots & \ddots \end{bmatrix}$$

with matrix A containing on the diagonal the energies of the eigenstates $|\alpha\rangle$ and matrix B built of the elements $\frac{i}{2} \langle \alpha | eF_0 z | \beta \rangle$.

We solve the eigenproblem of the Hamiltonian H_F and obtain a set of eigenenergies ϵ_l and eigenstates $|\epsilon_l\rangle$. Using the result we can calculate the time averaged (average over initial time t_0 and ac pulse duration $t - t_0$) probability of the transition between α and β states

$$P_{\alpha \rightarrow \beta} = \sum_n \sum_l |\langle \beta n | \epsilon_l \rangle \langle \epsilon_l | \alpha 0 \rangle|^2. \quad (15)$$

In order to obtain convergent results for the probabilities $P_{\alpha \rightarrow \beta}$ a sufficient number of the harmonics $\pm n\hbar\omega$ must be included into the H_F matrix.

III. SPECTRA IN EXTERNAL MAGNETIC FIELD

The single-carrier energy levels confined in the n - and p -type quantum dots are displayed in Fig. 4 and the calculated lowest energy levels of the (1e,1h) charge configuration in Fig. 5(a,b,c). The single-electron states occupied in the dominant configurations for the (1e,1h) states at $B = 0.1$ T are listed in Table I.

In the four lowest-energy (1e,1h) states of Fig. 5(a-c) – in the dominant configurations – two of the three electrons of the p dot occupy the two-lowest energy states of

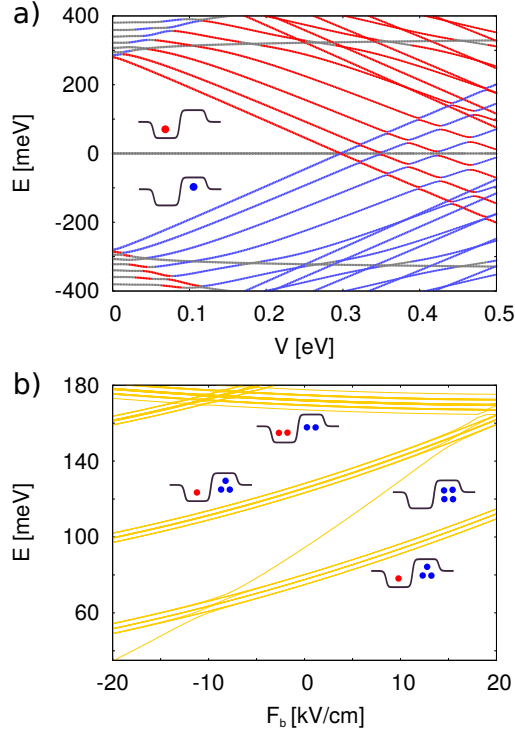


Figure 3. (a) Single electron energy levels as a function of the QD potentials $V = V_n = V_p$. Red/blue lines represent states with at least 40% of the wavefunction localized within the n/p dot. (b) Four electron energy levels as a function of bias electric field F_b for $V = 0.21$ eV. The insets explain the QD charge occupation corresponding to each set of the energy levels.

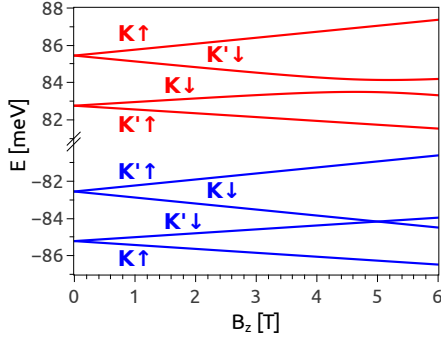


Figure 4. Energy of the dot-localized single electron states of the top of the valence (blue lines) band and the bottom of the conduction band (red lines) as a function of B_z .

the valence band ($pK\uparrow$ and $pK'\downarrow$ in Fig. 4). The third electron of the p dot occupies one of the two-highest energy levels of the valence band ($pK\downarrow$ or $pK'\uparrow$). Finally, the single electron in the n type dot occupies one of the two-lowest energy states of the conduction band ($nK\downarrow$ or $nK'\uparrow$). The low-energy spectrum at $B = 0$ [Fig. 5(a,b)] consists of a ground-state singlet and an excited state triplet. In the states denoted by B1 and B2 in Fig. 5 the last two electrons are spin-valley polarized, i.e. in

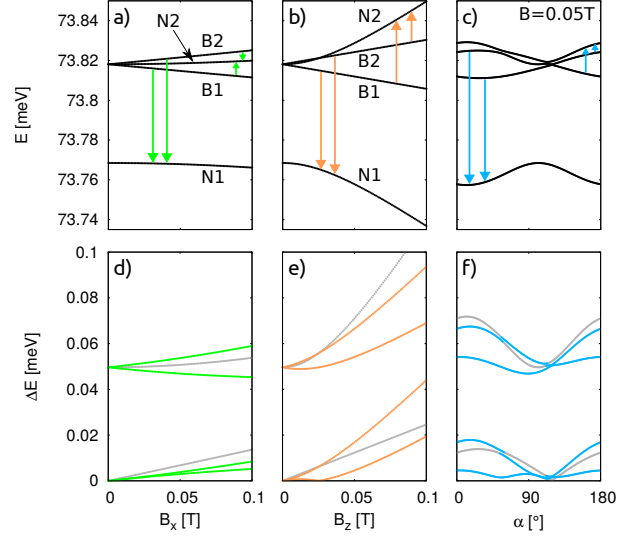


Figure 5. (a-c) Energy of the four-electron lowest-energy states as a function of B_x , B_z and α , respectively. The color arrows represent the transitions between Pauli blocked and nonblocked states. (d-f) Transition lines corresponding to the arrows on the plots (a-c).

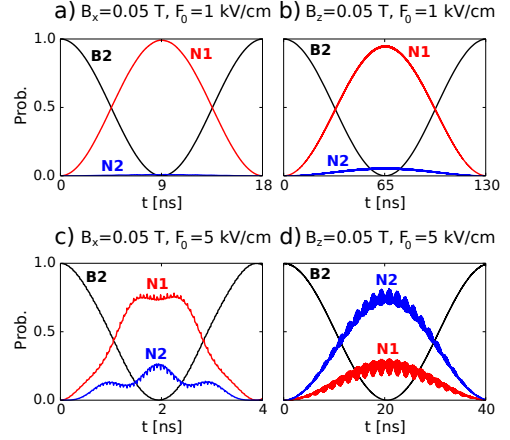


Figure 6. N1, N2 and B2 occupation probabilities during the B2 \rightarrow N1 resonant transition at four different magnetic fields and amplitudes of the ac electric field.

B1 the last electron in both n and p dot occupies the $K\uparrow$ energy level, and for B2 the occupied spin-valley level is $K'\uparrow$. Both these states are blocked, i.e. in terms of the *dominant* spin-valley configurations of Table I, the electron of the n dot is forbidden to pass to the p dot by the Pauli exclusion principle, since the state with the same spin and valley is occupied in the p dot. This is not the case for the other two states – denoted by N1 and N2 in Fig. 5. These states are referred to as “nonblocked” in the following. The nonblocked states enter into an avoided crossing that is opened at $B = 0$ by the exchange integral [14, 41], hence their non-linear dependence on B near 0T.

The orbital magnetic dipole moment due to the elec-

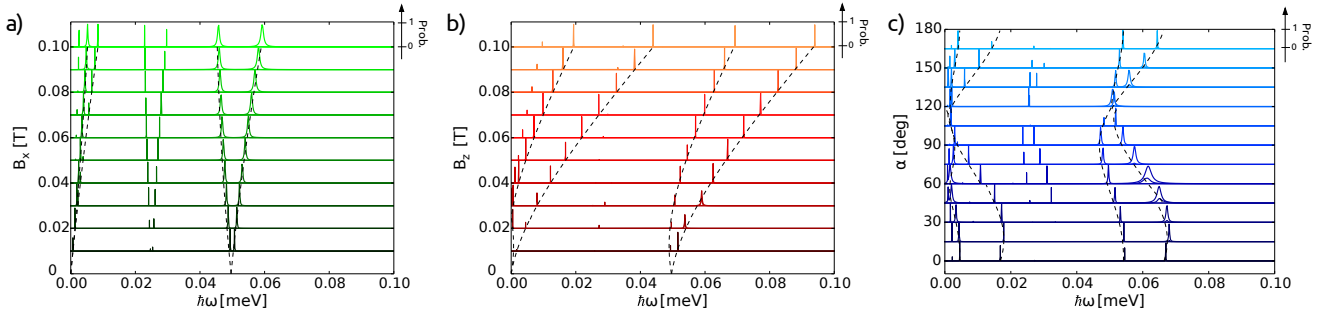


Figure 7. Maximal probability of the transition between Pauli blocked and non-blocked states (during 200 ns time evolution) as a function of the ac field frequency ω and (a) B_x , (b) B_z and (c) angle α for $B = 0.05$ T. The dashed lines indicate the $B \rightarrow N$ transition energies as calculated from the energy spectrum.

| (1e,1h) state | occupied single-electron states |
|---------------|--|
| N1 | pK \uparrow pK' \downarrow pK \downarrow nK' \uparrow |
| N2 | pK \uparrow pK' \downarrow pK' \uparrow nK \downarrow |
| B1 | pK \uparrow pK' \downarrow pK \downarrow nK \downarrow |
| B2 | pK \uparrow pK' \downarrow pK' \uparrow nK' \uparrow |

Table I. The dominant occupation of the single-electron energy levels of Fig. 4 in the lowest-energy (1e,1h) states of Fig. 5(a,b,c) for nonzero magnetic field ($B = 0.1$ T). The first column indicates the energy level of Fig. 5(a,b,c), and the remaining columns the energy levels occupied in the p and n type dot.

| | N1 | B1 | B2 | N2 | (0e,0h) |
|---------|----------------------|----------------------|----------------------|----------------------|----------------------|
| N1 | 15.84 | $9.53 \cdot 10^{-5}$ | $3.23 \cdot 10^{-4}$ | $2.12 \cdot 10^{-2}$ | 1.03 |
| B1 | $9.53 \cdot 10^{-5}$ | 15.79 | $1.62 \cdot 10^{-6}$ | $8.22 \cdot 10^{-5}$ | $2.94 \cdot 10^{-3}$ |
| B2 | $3.23 \cdot 10^{-4}$ | $1.62 \cdot 10^{-6}$ | 15.79 | $2.51 \cdot 10^{-4}$ | $7.31 \cdot 10^{-3}$ |
| N2 | $2.12 \cdot 10^{-2}$ | $8.22 \cdot 10^{-5}$ | $2.94 \cdot 10^{-3}$ | 15.80 | 0.433 |
| (0e,0h) | 1.03 | $2.94 \cdot 10^{-3}$ | $2.51 \cdot 10^{-4}$ | 0.433 | 33.12 |

Table II. Dipole matrix elements $\langle \psi_i | z | \psi_f \rangle$ between the energy levels marked in Fig. 5(b) by B1, B2, N1 and N2 for (1e,1h) charge configuration and the "vacuum state" (0e,0h) with no electrons in the n -dot and fully filled p -dot (4 electrons in the dot) for $B_z = 0.05$ T. The dominant Slater determinants for (1e,1h) states are indicated in Table I. The vacuum state (0e,0h) is the non-degenerate energy level that grows fastest with the bias field F_b in Fig. 3(b). The results are given in nanometers.

tron circulation around the tube [43] is oriented parallel or antiparallel to the axis of the tube [32]. Moreover, the circumferential spin-orbit interaction fixes the projection of the electron spin on the orbital magnetic moment [17]. Thus, the spins of the lowest-energy states are nearly polarized along the axis of the tube and a weak magnetic field applied in the x direction does not affect the energy levels of electrons confined within a straight CNT. The entire dependence of the energy levels on $\mathbf{B} = (B_x, 0, 0)$ that is visible in Fig. 5(a) results from the bent of the CNT. For the considered radii of the bent [R_n , R_p in Fig. 2] the reaction of the energy

levels on the magnetic field $\mathbf{B} = (0, 0, B_z)$ is still much stronger [Fig. 5(b)]. The reaction anisotropy to the magnetic field vector leads to the distinct dependence of the spectrum on the angle α that the vector \mathbf{B} forms with the z axis [Fig. 5(c)].

IV. SPIN-VALLEY TRANSITIONS

A. Weak ac field

The lifting of the Pauli blockade in states B1 and B2 is achieved via transitions to one of the states N1 or N2 [11, 12, 14, 15] – see the arrows in Fig. 5(a-c) – that is induced by the ac electric field. Figures 5(d-f) show the energy difference between the blocked and nonblocked B-N levels (color lines). For completeness, the energy difference between the blocked pair of energy levels B1-B2 (the gray line that starts at zero energy at $B = 0$) and unblocked N1-N2 levels (the higher energy gray line) were also plotted.

Figure 6 shows the time-resolved occupation probabilities obtained for the driving frequency set for the B2 \rightarrow N1 resonant transition with the electron initially in state B2. For a weak ac field amplitude of 1 kV/cm [Fig. 6(a,b)] the transition is much faster for the magnetic field that is oriented perpendicular to the axis of the CNT $\mathbf{B} = (B_x, 0, 0)$ than for $(0, 0, B_z)$. The transition from B2 to N1 involves both the valley and the spin inversion in pK' $\uparrow \rightarrow$ pK \downarrow [Table I]. For a straight CNT spins are polarized in the z or $-z$ directions. For B oriented along the x direction the energy change is weaker [Fig. 5(a)] but this field orientation contributes in mixing the σ_z eigenstates and to opening the channel for the spin inversion, hence the shorter transition times.

Figure 7 shows the maximal transition probability from B1 and B2 states to the nonblocked ones N1 and N2 as functions of the driving ac frequency for a number of magnetic field values [Fig. 7(a,b)] and orientation angles [Fig. 7(c)] for $F_0 = 1$ kV/cm – i.e. the one considered in Fig. 6(a,b). For each value of the magnetic field

in Fig. 7 we plot two curves for the initial state set at either B2 and B1. The dashed lines indicate the nominal transition energies which agree very well with the peaks position. We can see that the width of the lines for B_x is larger which is consistent with the shorter transition times [Fig. 6(a,b)] for the two-level Rabi transitions. For this – weak oscillations amplitude – considered in Fig. 7 (a) the g factors for the transitions can be exactly estimated from the energy spectra.

Let us briefly comment on the relation of the energy differences between the blocked and nonblocked energy levels and the experimental EDSR transitions (Fig. 2 of Ref. [12]): (i) The dependence over the orientation angle of the magnetic field in the (x, z) plane of both the experimental (Fig.2(c) of Ref. [12]) and the present (Fig. 5(f)) results exhibits a pair of lines near zero transition energy/frequency separated by a gap from another pair of levels. The lines change in phase with the maxima near 0 and 180° and a minimum near 0. (ii) In the upper pair of lines as a function of B_x [Fig. 2(a) of Ref. [12]] one of the lines increases and the other decreases with the magnetic field. The effective g factor extracted from the slope for the increasing line $g = \frac{1}{\mu_B} \frac{dE}{dB}$ of the experimental paper is 1.8 while for the data of Fig. 5 the value is 1.67 (we take the derivative near 0.05 T). For the decreasing line we find -0.68. Although no g factor estimate has been given for that line in the experiment, from Fig.4(h) in Ref. [15] we can assert that the slope of the decreasing line is less steep than for the increasing one, thus $|g| < 1.8$. For the lower lines we find g factors of 1.49 and 0.86, while the experimental data provides 1.9 for one of the lines. For nonzero B only a single lower line is resolved in the experiment. (iii) The largest deviation for the g factors is found for B_z orientation of the field: we find 8.67 and 4.42 for the g factors in the upper branch, while the experimental paper produces 4.5 and 3 respectively. A possible explanation for the deviation of the actual transition spectrum from the spacing derived from the energy spectrum is provided below.

B. Strongly driven system

We analyze an effect of an amplification of the ac driving field on the dynamics of the system. In Fig. 8 we plot the transition spectra for amplitudes $F_0 = 1, 2, \dots, 5$ kV/cm at two different magnetic field orientations – $B_x = 0.05$ T and $B_z = 0.05$ T. In both cases the increase of F_0 yields a few interesting effects: (i) broadening of the resonant peaks, (ii) shifts of the resonant transition energies (especially large for the upper branch lines), (iii) emergence of the $B2 \rightarrow N2$ transition at $B2 \rightarrow N1$ resonant peaks, and (iv) appearance of fractional resonances at the fractions of the resonant frequencies.

Widening of the resonant peaks is a signature of the acceleration of the transitions. For the case of Fig. 6(c,d) an increase of the ac electric field amplitude F_0 from 1 to 5 kV/cm shortens the transition time slightly

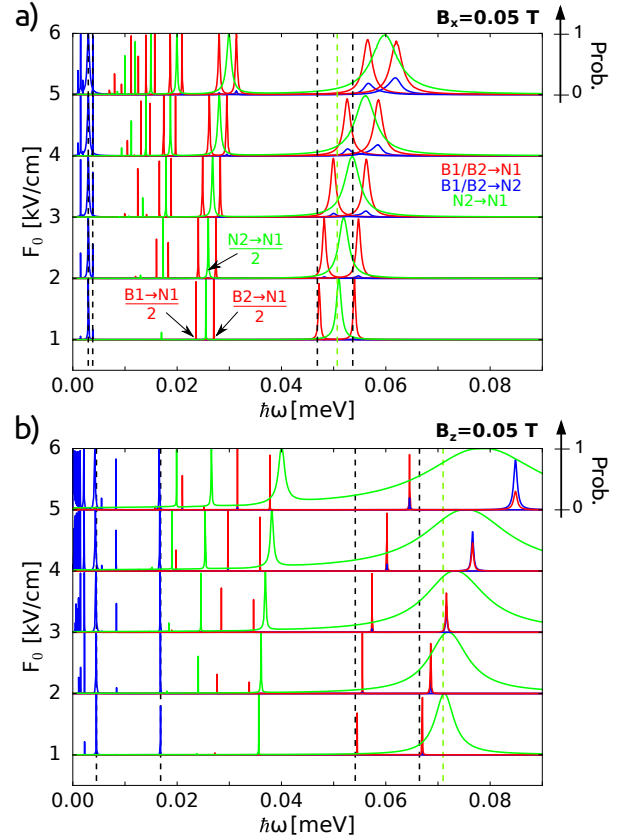


Figure 8. Maximal occupation probability obtained for a solution of the Schrödinger equation for 200 ns as a function of the driving field frequency and amplitude for (a) $B_x = 0.05$ T and (b) $B_z = 0.05$ T. The plots show the simulations for both B1, B2 set in the initial condition that evolve to N1 (red line) or N2 (blue line) states. The green line indicates the maximal occupation probability of N1 state for N2 in the initial condition. The dashed vertical line show the energy differences for $B \rightarrow N$ transition (black lines) and $N2 \rightarrow N1$ transition (green line).

less than 5 times. The ac frequency in Fig. 6(c,d) is targeted to $B2 \rightarrow N1$ transition. Nevertheless, one observes also an appearance of N2 energy level, although the $B2 \rightarrow N2$ transition is strongly off resonance with the driving frequency. The energy for the direct $B2 \rightarrow N2$ transition is 10 times smaller than to N1, and the dipole element for the transitions to N1 and N2 are similar [see Table II].

Note, that in Table II the dipole matrix elements between B and N states are non-zero only because of the small admixtures of the opposite spin and valley which appear in the single-electron states – indicated in Table I – due to the presence of the intervalley and spin-orbit coupling. The diagonal elements have an interpretation of the dipole moment of the state. For the quadruple of (1e,1h) states the dipole moment is similar, and for (0e,0h) it is larger which agrees with the slope of the energy levels in Fig. 3(b) with F_b .

Better insight into origin of the resonant frequency

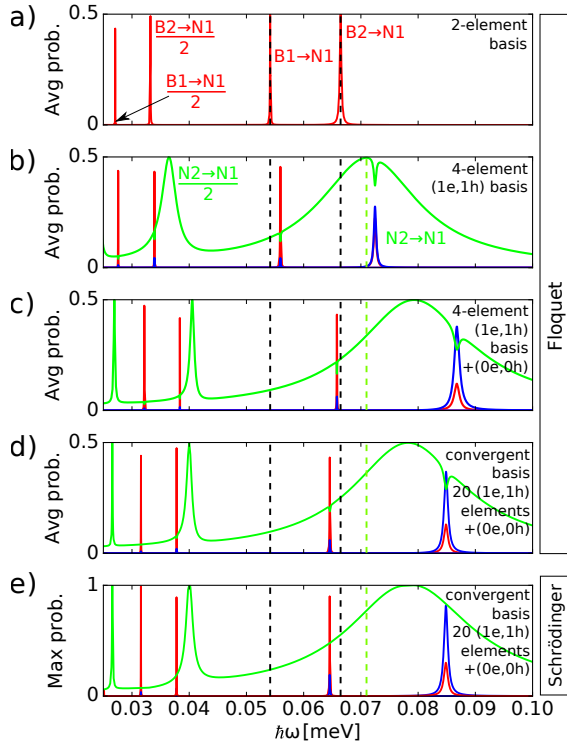


Figure 9. The transition spectra for $B_z = 0.05$ T and $F_0 = 5$ kV/cm for varied basis of few-electron stationary Hamiltonian eigenstates.

shifts can be provided by the analysis of the convergence of the basis. This can be useful also for the discussion of the appearance of N2 in the dynamics at the frequency which is set to transition to N1. Figure 9 presents the average occupation probability for $F_0 = 5$ kV/cm and $B_z = 0.05$ T as obtained from the Floquet theory and a growing number of basis elements. We can see that the transition spectrum gets blue-shifted from the two-level Rabi transition [Fig. 9(a)] with the inclusion of the entire quadruple (B1,B2,N1,N2) of the lowest-energy (1e,1h) levels [Fig. 9(b)]. Moreover formation of the two-photon resonance for N1→N2 transition is observed at half the frequency for the direct resonance. Inclusion of the vacuum state (0e,0h) (empty n dot, four electrons filling completely the p dot energy levels) as the fifth element to the basis provides even stronger blueshift and produces a spectrum nearly identical with the convergent one. The transitions are blue-shifted as in the Bloch-Siegert shift [18, 45], however the effects of Fig. 8 do not follow the dependence on F_0 for the Bloch-Siegert transitions since they involve more than two energy levels. Note, that for $B_z = 0.05$ T the order of the transition lines is changed with respect to the energy spectrum (dashed vertical lines): the N1→N2 transition enters between the B→N1 lines.

We can see that the electron tunneling from (1e,1h) quadruple to the nondegenerate (0e,0h) state has a pronounced effect on the transition spectrum. Analyzing

the right hand side of Eq. (7) we found (see Supplement [44]) that for the transitions of Fig. 6(c,d) (an exact basis and a resonant frequency was used) the electron from the initial state B2 is transferred most effectively to the vacuum state (0e,0h) – for which the transition matrix element [Table II] is the largest (the transition rate $B2 \rightarrow (0e,0h)$ is larger by an order of magnitude than for $B2 \rightarrow N$ transitions). Note, that this transition is off resonance, since the ac frequency in Fig. 6 is tuned to $B2 \rightarrow N1$ transition and the (0e,0h) state is for $F_b = 0$ about 20 meV higher in the energy [Fig. 3(b)] than the (1e,1h) ground-state. Note, that for the AC field with amplitude $F_0 = 5$ kV/cm the energy difference between the lowest-energy (1e,1h) state and the (0e,0h) state is quite large within the driving period and varies between 10 meV and 30 meV – see Fig. 3(b) for $F_b \in (-5, 5)$ kV/cm.

Beside the resonant $B2 \rightarrow N1$ transition, in Fig. 6(c,d) both N1 and N2 states get occupied by transitions from the vacuum state (0e,0h) – these states are more strongly coupled to the vacuum state (0e,0h) than to one other [Table II]. The vacuum state serves as an intermediate one for transitions to N1 and N2 states. The transition (0e,0h)→N1/N2 is immediate which prevents accumulation of the electron in the vacuum state (0e,0h). The (0e,0h) occupation probability in the conditions of Fig. 6(d) is 2‰ at most [see Fig. S1 in the Supplement [44]]. The transition $N2 \leftrightarrow N1$ is nearly in resonance with the driving frequency resonant for the $B2 \rightarrow N1$ transition, so for the conditions of Fig. 6(d) we find that $N2 \leftrightarrow N1$ transitions are by a factor of 1.5 to 2 more effective than for the $N \leftrightarrow (0e,0h)$ ones [see Fig. S2 in the Supplement [44]]. The N2 state has also been observed in Fig. 6(b) for the smaller amplitude of $F_0 = 1$ kV/cm. For this amplitude the vacuum state (0e,0h) does participate in the transition with adequately lower maximal occupation probability of about 0.05‰.

C. The effective g factors for transitions lifting the spin-valley blockade

The dependence of the transition spectra on the magnetic field is given in Fig. 10. Let us focus on the direct $B1/2 \rightarrow N1$ and $N2 \rightarrow N1$ transitions – the ones of the high energy branch of the plots. For B_x orientation of the field – the three maxima are blue-shifted with respect to the energy difference, but the shift does not strongly depend on the magnetic field. Hence, the effective g factors for the B_x orientation are similar to the ones obtained from the energy spectra – see the upper half of Table III. A slight reduction of the absolute value of the g factors is observed in the transition lines for $F_0 \geq 3$ kV/cm.

For the magnetic field oriented along the z axis the g factors deviate more significantly from the ones obtained from the energy spectra. In the energy spectra for B_z field the N2 level shifts promptly up the energy scale off B2 and B1 energy levels, and the transition $N2 \leftrightarrow N1$

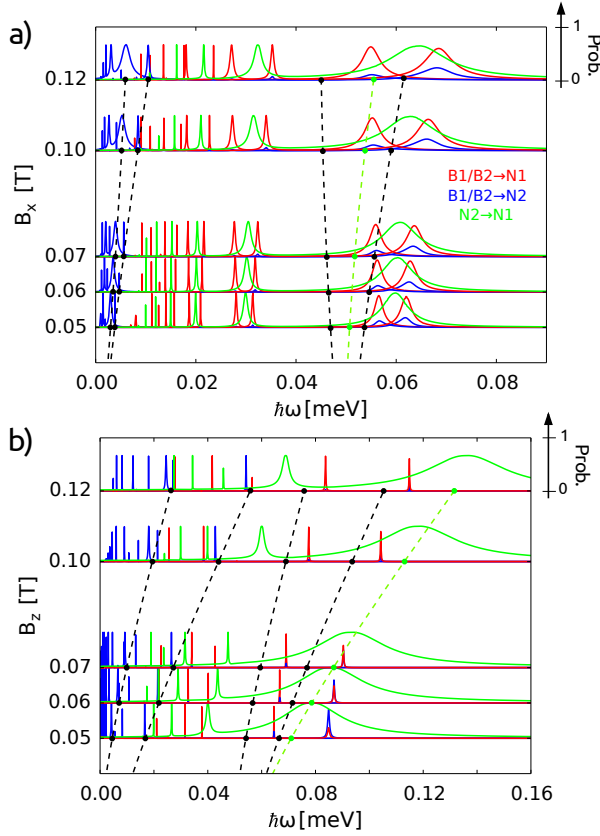


Figure 10. Maximal occupation probability obtained for a solution of the Schrödinger equation for 200 ns as a function of the driving field frequency and the magnitude of (a) B_x and (b) B_z magnetic field. The ac driving field amplitude was set to 5 kV/cm.

energy separates from $B \rightarrow N1$ energy – on contrary to what is observed for B_x field. When $N2 \leftrightarrow N1$ shifts off the $B1/2 \rightarrow N1$ transition energies, the blueshift of their energies is reduced, hence the reduction for the g factors (lower part of Table III). The g factors – as taken from the spectra were by a factor of 1.5 to 2 larger than in the experiments. The g factors as calculated from the transition spectra are significantly decreased for larger F_0 . Moreover, the values for both $B \rightarrow N1$ transitions produce similar g factors at larger F_0 – while from the energy spectra one was nearly 2 times larger than the other.

D. Detuning and the transition energy shifts

The reduction of the g factors discussed above has been obtained as a result of the energy shifts of the transition lines that occur for a relatively large amplitude of 5 kV/cm (potential drop of 0.5 mV along 100 nm), while in the experiment [12] the amplitude of 0.5 kV/cm was applied. The factor which is crucial in the energy shifts discussed above is the participation of the vacuum

| | | g factors for B_x | |
|--|--|-----------------------|---------------------|
| | | $B2 \rightarrow N1$ | $B1 \rightarrow N1$ |
| E spectrum | | 1.7 | -0.7 |
| transitions for $F_0 = 3$ kV / cm | | 1.6 | -0.6 |
| transitions for $F_0 = 5$ kV / cm | | 1.3 | -0.5 |
| experiment [12] | | 1.8 | - |
| | | g factors for B_z | |
| | | $B2 \rightarrow N1$ | $B1 \rightarrow N1$ |
| E spectrum | | 8.7 | 4.4 |
| transition lines for $F_0 = 3$ kV / cm | | 7.4 | 4.2 |
| transition lines for $F_0 = 5$ kV / cm | | 3.5 | 3.7 |
| experiment [12] | | 4.5 | 3 |

Table III. Effective Landé factors $g = \frac{1}{\mu_B} \frac{dE}{dB}$ for $B \rightarrow N1$ transitions for the magnetic field oriented in x (upper part) and z direction (lower part of the table) as calculated from energy and transition spectra and the experimental results of Ref. [12]. In the calculated results the derivative is taken at 0.05 T. Due to a finite width of the transition peaks – that are not strictly symmetric – at the energy scale – we estimate the precision in the evaluation of the g factors to ± 0.1 .

(0e,0h) state in the transitions, and it varies not only with the amplitude but also on the bias F_b between the dots. The latter shifts the position of the (0e,0h) state on the energy scale with respect to the (1e,1h) ground-state quadruple [Fig. 3(b)]. The position of these two states is controlled in the EDSR experiment by detuning voltage applied between the dots [4, 12].

The role of the detuning for the energy shifts can be estimated from Figure 11(a), where we plotted the result for $F_0 = 5$ kV/cm and $B_z = 0.05$ (same as Fig. 9(d)) but for $F_b = 10$ kV/cm. The (0e,0h) state is now about 40 meV above the (1e,1h) ground-state. The blueshift of the transition peaks with respect to the energy splitting is reduced from large [Fig. 8] to barely visible in Fig. 11(a). On the other hand – for $F_0 = 1$ kV/cm – for which the transition lines at $F_b = 0$ coincide with the energy differences (see Fig. 8(b) for $F_0 = 1$ kV/cm) for $F_b = -3$ kV/cm [the (0e,0h) state $\simeq 17$ meV above the (1e,1h) ground-state], the blue shifts appear – see Fig. 11(b). Concluding, the transition energy shifts that stand behind the variation of the g factors appear also for small amplitudes provided that the coupling with the (0e,0h) state is activated.

In the simulations the vacuum (0e,0h) state gets never very strongly occupied, and serves as a transition channel between the (1e,1h) energy levels of the lowest-energy quadruple. Nevertheless, the coupling between the vacuum (0e,0h) state and (1e,1h) states has a tunnelling character. The effects of the tunneling for a quantum wire – quantum dot in the EDSR phenomenon was studied in Ref. [46]. The authors [46] found that the spin flipping probability gets below 1 for stronger ac field and that the transition times are lower than expected for the Rabi oscillations. The first effect was encoun-

tered in Figs. 6(d) as according to the present study the effect results from participation of a third state in the dynamics. We also reproduce the other feature for larger ac fields. The $B2 \rightarrow N1$ transition time for these two states included in the basis for the results of Fig. 8(a) – which produces the Rabi transition mechanism – is 13 ns, while the spin-valley flip time for the convergent basis [Fig.8(e)] is 20 ns.

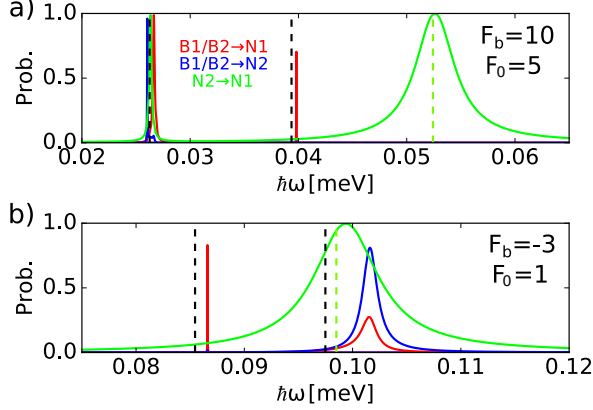


Figure 11. Maximal occupation probability obtained for a solution of the Schrödinger equation for 200 ns for $B_z = 0.05$ T and (a) $F_0 = 5$ kV/cm, $F_b = 10$ kV/cm, (b) $F_0 = 1$ kV/cm, $F_b = -3$ kV/cm.

E. Resonant transitions vs high harmonic generation

The results presented above contained a number of features characteristic to nonlinear optics. Besides the shifts of the direct transition lines also fractional resonances were observed, i.e. resonances at fractions of the direct transition frequency (see Fig. 9,8,10). These transitions correspond to multiphoton absorption that is observed in atomic optics at intense laser fields. For the gated nanodevices the conditions for observation of the phenomena characteristic to nonlinear optics [4, 15, 47] appear at decent excitations of the order of 1 kV/cm (or the potential drop of 1 mV over 100 nm). In gaseous phase [23] and in solids [24] strong laser fields ionize atoms and the ionized electrons are accelerated in the electric field of the laser. The oscillations of the dipole moment of the ionized electrons give rise to high harmonic generation [22] that is used in generation of ultrashort pulses [23].

We looked for high harmonics of the electron dipole moments that are driven by the ac field in our system [22]. We considered $F_0 = 1$ kV/cm, $B_z = 0.05$ T and no bias. Once the dynamics of the system is known we calculate the dipole moment $z_d(t) \equiv e\langle(z_1 + z_2 + z_3 + z_4)\rangle$. Next, we Fourier analyze the dependence of the dipole moment on time. The results are presented in Fig. 12. We set the initial state to B2 in Fig. 12(b,c)

and N2 in Fig. 12(d,e,f). The applied driving frequency of the electric field is taken resonant for the $B2 \rightarrow N1$ transition Fig. 12(b) and resonant for the direct Fig. 12(d) and two-photon 12(e) $N2 \rightarrow N1$ transitions as well as off resonances [Fig. 12(c,f)]. For resonant conditions we resolve up to 5th harmonic of the driving frequency [Fig. 12(b,d,e)]. Off resonances the highest harmonic of the spectrum is the 3rd one [Fig. 12(c,f)].

In off resonant conditions we notice a peak that correspond to the direct resonant transition $B2-N1$ [a tiny feature in Fig. 12(c)] and $N2-N1$ [a pronounced feature in Fig. 12(f)]. For the latter plot also other lines are observed. The $N2-N1$ transition line is wide at the energy scale and couples strongly to other transitions.

Note, that in strong laser fields the high harmonic generation is a non-resonant phenomenon [22–24]. In the present conditions the yield of the high harmonics is still strongly related to the resonant transition spectrum. In resonant conditions the 2nd harmonics is by one [Fig.12(e)], two [Fig.12(d)] or three orders [Fig.12(b)] of magnitude lower than the driving frequency. Off resonance the peak for the 2nd harmonic of the driving frequency is 4 [Fig.12(f)] or 6 [Fig.12(e)] orders of magnitude lower.

Obviously, high harmonics generated in our systems have only moderate order in comparison to HHG gener-

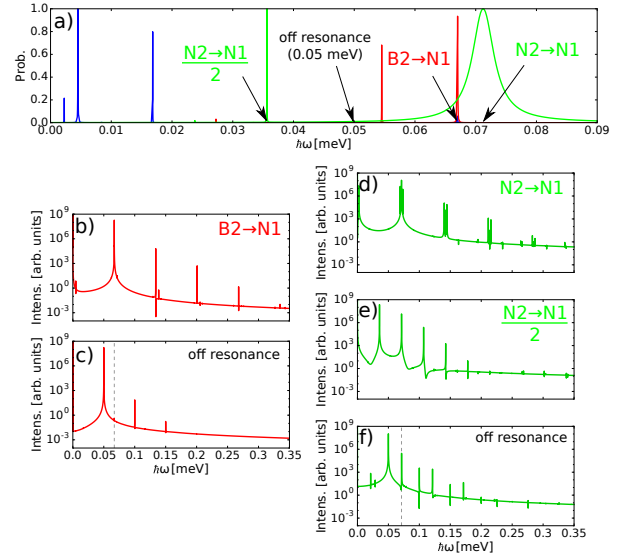


Figure 12. Fourier transform of the electron dipole moment for $F_0 = 1$ kV/cm and $B_z = 0.05$ T at no bias field. Panel (a) shows the driving frequencies $\hbar\omega_c$ considered in this plot. In (b) and (c) B2 is the initial state. In (b) the driving frequency is $\hbar\omega_{ac} = 0.067$ meV – resonant for the $B2-N1$ transition. In (c) $\hbar\omega_{ac} = 0.05$ meV we are off resonance. The dashed line in (b) shows the position of the resonant frequency of (b). In (d-f) the initial state is N2. In (d) and (e) resonant ac frequencies are set for the direct ($\hbar\omega_{ac} = 0.0712$ meV) and two-photon ($\hbar\omega_{ac} = 0.0356$ meV) $N2-N1$ transition. In (f) an off resonant driving frequency is applied ($\hbar\omega_{ac} = 0.05$ meV). The dashed line in (f) shows the position of the $N2-N1$ direct resonance frequency.

ated in atoms or molecules where the orders of 100 can be achieved [48]. Still, the new mechanism discussed by us, when optimized could in principle lead to generation of “truly high” harmonics.

V. SUMMARY AND CONCLUSIONS

We have analyzed spin-valley dynamics of the four last electrons in a n-p ambipolar quantum dot using a time dependent configuration interaction method and the Floquet theory based on the single-electron states determined with the atomistic tight-binding approach. We studied the transitions lifting the Pauli blockade of the current within a quadruple of lowest-energy states of the (1e,1h) charge configuration. We discussed the results in the context of the accessible experimental data.

We demonstrated that the dynamics is significantly influenced by the coupling of the states of the (1e,1h) charge configuration with the nondegenerate vacuum (0e,0h) state. The vacuum state serves as a channel for transitions inside the (1e,1h) subspace and its participation in the transitions is determined by both the amplitude of the ac electric field and the bias electric field.

The effect of the coupling are transitions energy shifts off the values expected from the eigenenergy spectra. A strong modification of the g factors characterizing the dependence of the transitions on external axial magnetic field. High harmonic generation in the electron dipole moment was found for resonant driving frequencies.

ACKNOWLEDGMENTS

This work was supported by the National Science Centre according to decision DEC-2013/11/B/ST3/03837. E.N.O. benefits from the doctoral stipend ETIUDA of the National Science Centre according to decision DEC-2015/16/T/ST3/00266 and the scholarship of Krakow Smoluchowski Scientific Consortium from the funding for National Leading Reserch Centre by Ministry of Science and Higher Education (Poland). Calculations were performed in the PL-Grid Infrastructure. M.L. and A.C. acknowledge Spanish MINECO grants (National Plan FOQUS No. FIS2013-46768-P and Severo Ochoa Excellence Grant No. SEV-2015-0522), the Catalan AGAUR grant SGR 874 2014-2016, and Fundació Privada Cellex Barcelona.

-
- [1] I. Žutic, J. Fabian, and S. Das Sarma, *Rev. Mod. Phys.* **76**, 323 (2004).
 - [2] F. H. L. Koppens, C. Buizert, K. J. Tielrooij, I. T. Vink, K. C. Nowack, T. Meunier, L. P. Kouwenhoven, and L. M. K. Vandersypen, *Nature* **442**, 766 (2006).
 - [3] S. Nadj-Perge, V. S. Pribiag, J. W. G. van den Berg, K. Zuo, S. R. Plissard, E. P. A. M. Bakkers, S. M. Frolov, and L. P. Kouwenhoven, *Phys. Rev. Lett.* **108**, 166801 (2012).
 - [4] J. Stehlik, M. D. Schroer, M. Z. Maialle, M. H. Degani, and J. R. Petta, *Phys. Rev. Lett.* **112**, 227601 (2014).
 - [5] M. D. Schroer, K. D. Petersson, M. Jung, and J. R. Petta, *Phys. Rev. Lett.* **107**, 176811 (2011).
 - [6] E. I. Rashba and A. L. Efros, *Phys. Rev. Lett.* **91**, 126405 (2003); V. N. Golovach, M. Borhani, and D. Loss, *Phys. Rev. B* **74**, 165319 (2006).
 - [7] E. A. Laird, C. Barthel, E. I. Rashba, C. M. Marcus, M. P. Hanson, and A. C. Gossard, *Phys. Rev. Lett.* **99**, 246601 (2007); E. A. Laird, C. Barthel, E. I. Rashba, C. M. Marcus, M. P. Hanson, and A. C. Gossard, *Semicond. Sci. Tech.* **24** 064004 (2009).
 - [8] F. Forster, M. Mühlbacher, D. Schuh, W. Wegscheider, and S. Ludwig, *Phys. Rev. B* **91**, 195417 (2015).
 - [9] E. N. Osika, B. Szafran, and M. P. Nowak, *Phys. Rev. B* **88**, 165302 (2013).
 - [10] F. H. L. Koppens, J. A. Folk, J. M. Elzerman, R. Hanson, L. H. Willems van Beveren, I. T. Vink, H. P. Tranitz, W. Wegscheider, L. P. Kouwenhoven, and L. M. K. Vandersypen, *Science* **309**, 1346 (2005); A. C. Johnson, J. R. Petta, C. M. Marcus, M. P. Hanson, and A. C. Gossard, *Phys. Rev. B* **72**, 165308 (2005).
 - [11] F. Pei, E. A. Laird, G. A. Steele, and L. P. Kouwenhoven, *Nature Nano.* **7**, 630 (2012).
 - [12] E. A. Laird, F. Pei, and L. P. Kouwenhoven, *Nature Nano.* **8**, 565 (2013).
 - [13] A. Pályi and G. Burkard, *Phys. Rev. B* **82**, 155424 (2010).
 - [14] E. N. Osika and B. Szafran, *Phys. Rev. B* **93**, 165304 (2016).
 - [15] Y. Li, S. C. Benjamin, G. A. D. Briggs, and E. A. Laird, *Phys. Rev. B* **90**, 195440 (2014).
 - [16] G. Széchenyi and A. Pályi, *Phys. Rev. B* **88**, 235414 (2013); *Phys. Rev. B* **91**, 045431 (2015).
 - [17] F. Kuemmeth, S. Ilani, D. C. Ralph, and P. L. McEuen, *Nature* **452**, 448 (2008).
 - [18] J. H. Shirley, *Phys. Rev.* **138**, B979 (1965).
 - [19] S.-I. Chu and D. A. Telnov, *Physics Reports* **390**, 1 (2004).
 - [20] J. Romhányi, G. Burkard, and A. Pályi, *Phys. Rev. B* **92**, 054422 (2015).
 - [21] J. Danon and M. S. Rudner, *Phys. Rev. Lett.* **113**, 247002 (2014).
 - [22] M. Lewenstein, Ph. Balcou, M. Y. Ivanov, A. L’Huillier, and P. B. Corkum, *Phys. Rev. A* **49**, 2117 (1994).
 - [23] F. Krausz and M. Ivanov, *Rev. Mod. Phys.* **81**, 163 (2009).
 - [24] M. Schultze, E. M. Bothschafter, A. Sommer, S. Holzner, W. Schweinberger, M. Fiess, M. Hofstetter, R. Kienberger, V. Apalkov, V. S. Yakovlev, M. I. Stockman, and F. Krausz, *Nature* **493**, 75 (2013); T. T. Luu, M. Garg, S. Yu. Kruchinin, A. Moulet, M. Th. Hassan, and E. Goulielmakis, *Nature* **521**, 498 (2015); H. Hohenleutner, F. Langer, O. Schubert, M. Knorr, U. Huttner, S. W. Koch, M. Kira, and R. Huber, *Nature* **523**, 572 (2015).
 - [25] S. Neppl, R. Ernstorfer, A. L. Cavalieri, C. Lemell, G. Wachter, E. Magerl, E. M. Bothschafter, M. Jobst, M.

- Hofstetter, U. Kleineberg, J. V. Barth, D. Menzel, J. Burgdörfer, P. Feulner, F. Krausz, and R. Kienberger, *Nature* **517**, 342 (2015); G. Vampa, T. J. Hammond, N. Thiré, B. E. Schmidt, F. Légaré, C. R. McDonald, T. Brabec, and P. B. Corkum, *Nature* **522**, 462 (2015); G. Ndabashimiye, S. Ghimire, M. Wu, D. Browne, K. Schafer, M. Gaarde, and D. Reis, *Nature* **534**, 520 (2016).
- [26] E. N. Osika, A. Chacón, L. Ortmann, N. Suárez, J. A. Pérez-Hernández, B. Szafran, M. F. Ciappina, F. Sols, A. S. Landsman, and M. Lewenstein, arXiv:1607.07622;
- [27] M. F. Ciappina, J. A. Pérez-Hernández, A. S. Landsman, W. Okell, S. Zherebtsov, B. Förg, J. Schütz, J. L. Seiffert, T. Fennel, T. Shaaran, T. Zimmermann, A. Chacón, R. Guichard, A. Zaïr, J. W. G. Tisch, J. P. Marangos, T. Witting, A. Braun, S. A. Maier, L. Roso, M. Krüger, P. Hommelhoff, M. F. Kling, F. Krausz, and M. Lewenstein, arXiv:1607.01480.
- [28] K. Flensberg, and C. M. Marcus, *Phys. Rev. B* **81**, 195418 (2010).
- [29] T. S. Jespersen, K. Grove-Rasmussen, J. Paaske, K. Muraki, T. Fujisawa, J. Nygård, and K. Flensberg, *Nature Physics* **7**, 348 (2011).
- [30] P. Jarillo-Herrero, J. Kong, H. S. J. van der Zant, C. Dekker, L. P. Kouwenhoven, and S. De Franceschi, *Phys. Rev. Lett.* **94**, 156802 (2005).
- [31] L. Chico, M. P. López-Sancho, and M. C. Muñoz, *Phys. Rev. Lett.* **93**, 176402 (2004).
- [32] E. A. Laird, F. Kuemmeth, G. A. Steele, K. Grove-Rasmussen, J. Nygård, K. Flensberg, and L. P. Kouwenhoven, *Rev. Mod. Phys.* **87**, 703 (2015).
- [33] J. Klinovaja, M. J. Schmidt, B. Braunecker, and D. Loss, *Phys. Rev. B* **84**, 085452 (2011).
- [34] M. del Valle, M. Margańska, and M. Grifoni, *Phys. Rev. B* **84**, 165427 (2011).
- [35] T. Ando, *J. Phys. Soc. Jpn.* **69**, 1757 (2000).
- [36] G. A. Steele, F. Pei, E. A. Laird, J. M. Jol, H. B. Meerwaldt, and L. P. Kouwenhoven, *Nature Commun.* **4**, 1573 (2013).
- [37] E. N. Osika and B. Szafran, *J. Phys.: Condens. Matter* **27**, 435301 (2015).
- [38] D. Tománek and S. G. Louie, *Phys. Rev. B* **37**, 8327 (1988).
- [39] S. Schulz, S. Schumacher, and G. Czycholl, *Phys. Rev.* **73**, 245327 (2006).
- [40] P. Potasz, A. D. Güçlü, and P. Hawrylak, *Phys. Rev. B* **82**, 075425 (2010).
- [41] E. N. Osika and B. Szafran, *Phys. Rev. B* **91**, 085312 (2015).
- [42] A. Secchi and M. Rontani, *Phys. Rev. B* **88**, 125403 (2013).
- [43] T. S. Jespersen, K. Grove-Rasmussen, K. Flensberg, J. Paaske, K. Muraki, T. Fujisawa, and J. Nygård, *Phys. Rev. Lett.* **107**, 186802 (2011).
- [44] Supplementary information.
- [45] F. Bloch and A. Siegert, *Phys. Rev.* **57**, 522 (1940).
- [46] D. V. Khomitsky, L. V. Gulyaev, and E. Ya. Sherman, *Phys. Rev. B* **85**, 125312 (2012).
- [47] A. Mavalankar, T. Pei, E. M. Gauger, J. H. Warner, G. A. D. Briggs, and E. A. Laird, *Phys. Rev. B* **93**, 235428 (2016).
- [48] T. Brabec and F. Krausz, *Rev. Mod. Phys.* **72**, 545 (2000).

Spin-valley dynamics of electrically driven ambipolar carbon-nanotube quantum dots - Supplementary material

E.N. Osika,¹ A. Chacón,² M. Lewenstein,^{2,3} and B. Szafran¹

¹*AGH University of Science and Technology, Faculty of Physics and Applied Computer Science,
al. Mickiewicza 30, 30-059 Kraków, Poland*

²*ICFO - Institut de Ciències Fotoniques, The Barcelona Institute
of Science and Technology, 08860 Castelldefels (Barcelona), Spain*

³*ICREA, Pg. Lluís Companys 23, 08010 Barcelona, Spain*

This supplementary material contains additional analysis of the role of the vacuum state (0e,0h) and the emergence of B2 \rightarrow N2 transition for ac driving frequency to B2 \rightarrow N1 resonance for $B_z = 0.05$ T and $F_0 = 5$ kV/cm – as in Fig. 6(d) of the paper. We limited the basis to the 5 states: N1,B1,B2,N2,(0e,0h) that govern the dynamics of the system [see the convergence test of Fig. 9 in the paper]. In Fig. S1 we repeat a very beginning of the simulation presented in Fig. 6(d) only using the limited basis. We plot the vacuum state (0e,0h) occupation – previously omitted. The occupation of the vacuum state appears in peaks which are followed by a step of the occupation of the N2 state.

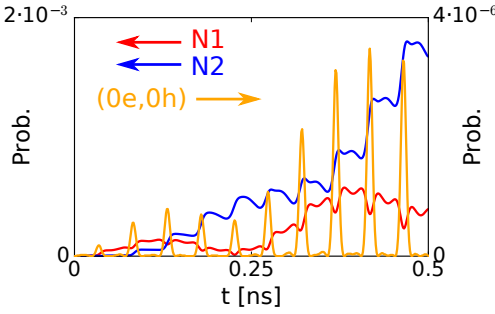


Figure S1. N1, N2 and (0e,0h) occupation probability at the beginning of the B2 \rightarrow N1 resonant transition at $B_z = 0.05$ T and $F_0 = 5$ kV/cm and the limited basis.

The role of the vacuum state (0e,0h) in the dynamics of the system can be followed by an analysis of the so-

lution of the Schrödinger equation in the configuration interaction method

$$i\hbar\dot{c}_k(t) = \sum_n c_n(t) eF_0 \sin(\omega t) \langle \Psi_k | z | \Psi_n \rangle e^{-\frac{i(E_n - E_k)t}{\hbar}}. \quad (1)$$

We integrate both sides over time with limits 0 and τ and obtain

$$\begin{aligned} c_k(\tau) &= c_k(0) + \\ &\frac{1}{i\hbar} \int_0^\tau \sum_n c_n(t) eF_0 \sin(\omega t) \langle \Psi_k | z | \Psi_n \rangle e^{-\frac{i(E_n - E_k)t}{\hbar}} dt \equiv \\ &c_k(0) + \sum_n J_{kn}(\tau), \end{aligned} \quad (2)$$

The integrated matrix elements $J_{kn}(\tau)$ contain information on the transitions between the basis states.

In Fig. S2 we label the five states of the limited basis [N1,B1,B2,N2,(0e,0h)] by their energy order in the spectrum as 1-st,2-nd,3-rd,4-th and 17-th state in the basis, respectively. In the initial condition the system occupies state B2 (i.e. the 3rd one). The third column of Fig. S2 indicates that the driving – resonant with B2 \rightarrow N1 transition (or 3 \rightarrow 1) induces most effectively the transition to the vacuum state (0e,0h) (17-th). The transition flux $J_{17,4}$ is about 30 times more effective than $J_{1,4}$. The last column of Fig. S2 shows that transitions from the vacuum state go to both N1 (1st) and N2 (3rd) states. The direct transitions between the N1 and N2 states are by 1.5 or 2 more effective than N \leftrightarrow (0e,0h) transitions – cf. $J_{4,1}$ and $J_{4,17}$ and $J_{17,4}$ and $J_{17,1}$, etc.

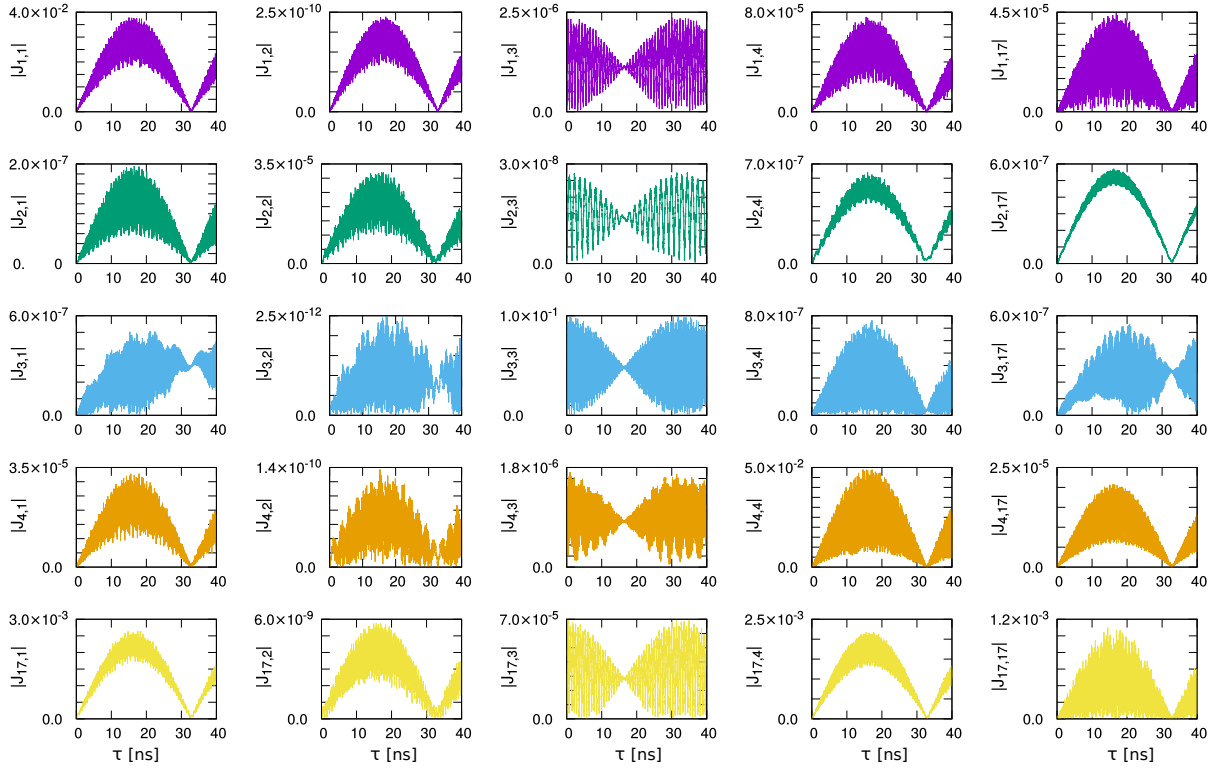


Figure S2. $|J_{kn}|$ elements as a function of τ for the driving frequency set in resonance to B2 \rightarrow N1 transition at $B_z = 0.05$ T and $F_0 = 5$ kV/cm.